PCCP

PAPER

View Article Online
View Journal

Cite this: DOI: 10.1039/c5cp00729a

Type VIII Si based clathrates: prospects for a giant thermoelectric power factor†

Payam Norouzzadeh,[ac] Jerzy S. Krasinski,[a] Charles W. Myles[b] and Daryoosh Vashaee*[c]

Received 5th February 2015,
Accepted 12th February 2015

DOI: 10.1039/c5cp00729a

www.rsc.org/pccp

Although clathrate materials are known for their small thermal conductivity, they have not shown a large thermoelectric power factor so far. We present the band structures of type VIII Si, Ge, and Sn clathrates as well as the alkali and alkaline-earth intercalated type VIII Si clathrates. Our calculations revealed that this group of materials has potentially large power factors due to the existence of a large number of carrier pockets near their band edges. In particular, we calculated the charge carrier transport properties of Si_{46}-VIII both for n-type and p-type materials. The exceptionally high multi-valley band structure of Si_{46}-VIII near the Fermi energy due to the high crystallographic symmetry resulted in a giant power factor in this material. It was shown that the intercalation of Si_{46}-VIII with alkali and alkaline-earth guest atoms shifts the Fermi energy close to the conduction band edge and, except for Be_8Si_{46} and Mg_8Si_{46}, they weakly influence the band structure of Si_{46}. Among these clathrate systems, Ca_8Si_{46}, Sr_8Si_{46}, and Ba_8Si_{46} showed negative formation energy, which should facilitate their synthesis. Our results imply that the intercalation affects the conduction band of Si_{46}-VIII more than its valence band. Also, interestingly, the type VIII clathrates of Si_{46} and its derivatives (except Be_8Si_{46} and Mg_8Si_{46}), Sn_{46}, and Ge_{46} all have 26 carrier pockets near their valence band edge. Among the different derivatives of Si_{46}-VIII, Rb_8Si_{46} and Ba_8Si_{46} have the highest number of electron pockets near their band edges. The thermoelectric power factor was predicted using a multiband Boltzmann transport equation linked with parameters extracted from density functional calculations. It was shown that both the increment of charge mobility and the existence of multiple band extrema contribute to the enhancement of the thermoelectric power factor considerably. Such a large power factor along with their inherently low thermal conductivity can make this group of clathrates promising thermoelectric materials.

I. Introduction

The clathrate compounds are expected to be very promising as high performance thermoelectrics not only due to their low thermal conductivity but also for their good charge carrier mobility.[1] In clathrates, the type and concentration of the guest metal atoms can be adjusted to modify their thermal and electrical properties. Moreover, the cage shape of a clathrate compound gives rise to a glass-like thermal conduction due to the effective phonon scattering by the rattling vibration of the guest atoms.[2] It is worth noting that not only the rattlers in the clathrate framework but also the open nature of the framework lead to low lattice thermal conductivity.[3]

Type-I and type-II clathrates based on Si, Ge and Sn elements have been studied extensively.[4–10] The first clathrate phases of silicon type-I and type-II were synthesized over 45 years ago by the extraction form alkali-metal silicides.[11] As far as we know, only six clathrate compounds with type-VIII structure have been synthesized so far, including $Eu_8Ga_{16}Ge_{30}$,[12] $Ba_8Ga_{16}Ge_{30}$,[7] $Sr_8Ga_{16-x}Al_xGe_{30}$ ($6 < x < 10$),[13] $Ba_8Ga_{16-x}Cu_xSn_{30}$ ($0 < x < 0.033$),[14] $Sr_8Ga_{16-x}Al_xSi_{30}$ ($8 < x < 10$),[15] and $Sr_8Ga_xSi_{46-x}$.[16–18] Nevertheless, none showed a large thermoelectric power factor. The following facts motivated us to systematically investigate the band structure and the thermoelectric power factor of the type-VIII Si-based clathrates. First, in our recent study we showed that the band structure of Si_{46}-VIII has an interestingly large number of closely packed electron pockets near both the conduction and valence band edges.[19] As we know, the large density of states near the band edges leads to a high thermoelectric power factor (>0.004 W m^{-1} K^{-2}).[19] The parental Si_{46}-VIII is a good starting material to engineer Si-based clathrate thermoelectric materials and the choice of rattling atoms or the cage substitutions can adjust the transport properties of clathrates.[20–26] Second, the p-type

[a] Helmerich Advanced Technology Research Center, School of Electrical and Computer Engineering, Oklahoma State University, Tulsa, OK 74106, USA
[b] Department of Physics, Texas Tech University, Lubbock, Texas 79409-1051, USA
[c] Monteith Research Center, Department of Electrical and Computer Engineering, North Carolina State University, Raleigh, NC 27606, USA.
E-mail: dvashae@ncsu.edu; Tel: +1-919-515-9599

† Electronic supplementary information (ESI) available. See DOI: 10.1039/c5cp00729a

type-VIII clathrates generally show higher Seebeck coefficients than that of type-I structures while having moderate electrical conductivity.[27] Third, the type-VIII clathrates have carriers with smaller effective masses and higher mobilities compared to those of type-I clathrates.[28] Therefore, considering the usually low thermal conductivity of clathrates, the type-VIII clathrates are expected to result in a high ZT.[27,29] Kishimoto *et al.* have also shown experimentally that $Sr_8Al_xGa_{16-x}Si_{30}$ type-VIII clathrates have higher mobility than type-I (24 $cm^2\ V^{-1}\ s^{-1}$ at 300 K compared to 5 $cm^2\ V^{-1}\ s^{-1}$).[30] The similar enhancements of the mobility in type-VIII clathrates compared to type-I systems have been reported for $Eu_8Ga_{16}Ge_{30}$ and $Eu_8Ga_xGe_{46-x}$.[15,31] Moreover, the optimally p-type doped $Eu_8Ga_{16}Ge_{30}$-VIII clathrate was predicated to have $ZT \propto \approx 1.2$ at 400 K.[32] These findings suggested that the type-VIII silicon based clathrates may have better charge transport performance than their type-I counterparts.

Our goal in the present study was to find if the electronic structures of type-VIII Si-based clathrates are appropriate for thermoelectric purposes. We try to provide a systematic insight into the charge transport properties of type-VIII Si-based clathrates. We studied the charge transport properties of this clathrate system in more detail, as it seems the most promising material among the materials considered in this study. To the best of our knowledge, none of the materials studied in this work have been synthesized yet and no computational study has been reported for their charge transport properties. However, the electronic structure, elastic, vibrational and thermodynamic properties of Si_{46}-VIII have been discussed in our previous study.[19]

The efficiency of a thermoelectric device relies on the average temperature difference and the thermoelectric figure-of-merit $ZT = S^2\sigma/kT$ where S, σ, T and k are thermopower, electrical conductivity, temperature, and lattice thermal conductivity, respectively. The material parameters appearing in the figure-of-merit ZT, such as thermopower and electrical conductivity, are coupled to the electronic structure of the material and cannot be optimized independently. Materials with multi-valley band structures can be potentially better thermoelectrics as all the band extrema that are close to the Fermi energy contribute to the enhancement of the power factor.

We modeled the role of each band extremum in order to gain insight into the possible enhancement of the figure-of-merit ZT by optimization of the carrier concentration for such clathrate materials. We apply a two-band semi-empirical model, which considers the characteristics of charge carriers and acoustic phonons. The main inputs of the model are the band structure parameters, doping concentration and range of temperature. The rest of the physical parameters are given in Table 1.

The applied multi-band model would be highly useful for engineering applications due to its simplicity. Moreover, the presented model can explain the electrical properties of clathrate Si_{46}-VIII and give a qualitatively reliable conclusion. The results would be beneficial for the analysis of future experimental data and can be utilized to design optimized thermoelectric materials.

Table 1 Si_{46}-VIII physical parameters used in the model

Parameter	Value
Debye temperature (K)	549
Static dielectric constant	12.14
High frequency dielectric constant	12.05
Sound velocity (m s^{-1})	5196
Lattice constant (Å)	10.1
Mass density (kg m^{-3})	2.082×10^3
Energy gap (eV)	1.24
Conduction band (CB) effective mass-ΓH line	(0.89 0.89 0.49)
Conduction band (CB) effective mass-HN line	(0.7 0.7 0.55)
Conduction band (CB) effective mass-Γ point	(0.315 0.315 0.315)
Valence band (VB) effective mass-ΓH line	(0.75 0.56 0.56)
Valence band (VB) effective mass-HN line	(1.58 0.52 0.52)
Valence band (VB) effective mass-N point	(2.29 0.29 0.29)
Valence band (VB) effective mass-P point	(0.76 0.76 0.76)
Valence band (VB) effective mass-Γ point	(0.45 0.45 0.45)
CB acoustic phonon deformation potential (eV)	*10*
VB acoustic phonon deformation potential (eV)	*10*

This study also describes a predictive and quantitative theoretical calculation of the energy band structure of type-VIII Si clathrates intercalated with alkali and alkaline-earth metals. In the ESI,† the main relaxation times employed in our model are described. Computational methodology is introduced in Section II. Section III gives the details of the modeling processes of the charge carriers. The calculated results along with discussions are presented in Section IV. The conclusions are given in Section V.

II. Computation methodology

A first-principles density functional plane wave method was applied for the calculation of energy band structures.[33] We employed the generalized gradient approximation (GGA) within the framework of density functional theory (DFT). To approximate the electron exchange–correlation energy, the Perdew–Burke–Ernzerhof functional was utilized.[34] The effect of core and semicore electrons was approximated by using ultrasoft pseudopotentials.[35] We did not include the spin–orbit coupling due to its negligible effect on the thermoelectric properties of light materials.[36] The energy cutoff for the plane wave basis was set to 400 eV and the Brillouin zone integration calculations were carried out over a $4 \times 4 \times 4$ Monkhorst–Pack k-point grid for all the structures. The total energy convergence was set to remain better than 10^{-6} eV. Only a single unit cell was employed in the calculations since the clathrate unit cell is large (46 atoms for pristine structures and 54 atoms for binary clathrates). We fully relaxed the geometry of all the clathrate structures. The electronic band structures were evaluated using the results of the structural relaxation calculations.

The main input parameters used in the model can be categorized into two sets. The entire first set of main parameters, such as the band structure and the lattice properties parameters (normal text in Table 1), was derived from the density functional theory calculations of electronic structure as well as the elastic and vibrational properties of clathrate Si_{46}-VIII, which were reported elsewhere.[19] The values of the

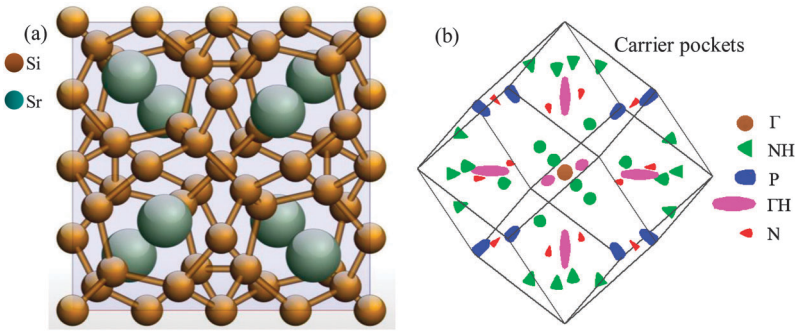

Fig. 1 (a) Sr_8Si_{46} as a typical crystal structure of guest-containing type-VIII clathrates. The framework atoms occupy 2a, 12d, 8c, and 24g sites and the guest atoms occupy 8c sites. (b) Brillouin zone of the Si_{46}-VIII clathrate. The hole pockets are shown at Γ = (0,0,0) point (brown), on the NH line (green), at P = (1/4,1/4,1/4) point (blue), on the ΓH line (violet), and at N = (1/2,0,0) points (red). The degeneracy of Γ, N, P, ΓH and NH is 1, 6, 2, 6, and 12, respectively.

second set of the parameters (text italic in Table 1) were estimated from their typical values for silicon based semiconductors. It should be noted that the three numbers in parentheses presented in Table 1 are the principal effective masses $(m_1, m_2, m_3) \times m_e$ in which m_e is the effective mass of the free electron. It is interesting to note that in Si_{46}-VIII, the clathrate holes have lighter effective mass than electrons. There are also a higher number of valleys close to the band edges in the valence band compared to the conduction band. As we will discuss, these two characteristics will result in a significantly higher thermoelectric power factor in p-types compared to n-types. We ignored the energy gap change with temperature in the calculations. The non-parabolicity parameters were calculated using a dense $8 \times 8 \times 8$ mesh around each selected k-point. We included the non-isotropic nature of the effective mass using mass tensors for each valley in the calculations.

The static and high frequency dielectric constants have been computed for Si_{46}-VIII using a linear response technique through density functional perturbation theory in VASP code as implanted in MedeA, which is described in the supporting information.[37–39]

We performed calculations *versus* doping concentration and temperature to find the optimal values. The model accounts for two bands (one valence band and one conduction band) in order to determine the charge transport properties of clathrate Si_{46}-VIII over a wide range of doping concentrations and temperatures.

III. Modeling processes

The first step in the calculation procedure is solving the charge conservation condition to find the Fermi level *versus* the temperature and doping concentration. In the second step, the scattering rates for charge carriers as described in the supporting information were computed. The dominant scattering mechanisms in crystalline Si_{46}-VIII are due to the acoustic phonons and ionized impurities. The relaxation times were calculated for acoustic phonon and ionized impurity scattering mechanisms and were combined using the well-known Matthiessen's rule to calculate the thermoelectric properties of clathrate Si_{46}-VIII. The main TE properties, such as the charge carrier mobility, Seebeck coefficient, and electrical conductivity, were calculated by solving the multi-band multi-valley Boltzmann transport equation. The main thermoelectric properties such as the electrical conductivity, Seebeck coefficient, and electronic thermal conductivity can be calculated as explained in the supporting information. Finally, we calculated the Lorentz number *versus* temperature. The energy gap was calculated by the DFT-GGA method as aforementioned. The effective masses were obtained by fitting the energy bands to a quadratic polynomial.[19] According to the numerical scheme described above, most of the required parameters for the calculation of charge transport properties of Si_{46}-VIII were derived from first principles DFT based calculations.

IV. Results and discussion

Electronic band structure of alkali and alkaline-earth intercalated type-VIII Si_{46} clathrates

The type-VIII clathrates have the space group $I\bar{4}3m$ (No. 217). The unit cell of Sr_8Si_{46} is shown in Fig. 1(a). In Sr_8Si_{46}, Sr atoms are encapsulated in cages comprising 23 atoms of Si. The framework atoms occupy four Wyckoff sites, 2a, 12d, 8c, and 24g, and the Sr guest atoms (indicated by Sr in the figure) occupy the 8c Wyckoff positions.[41] Fig. 1(b) presents 6 pockets along the ΓH line inside the Brillouin zone and 24 half-pockets along the NH line (green), one pocket at the Γ = (0,0,0) point, 8 quarter-pockets at P = (1/4,1/4,1/4) points and 12 half-pockets at N = (1/2,0,0) points. Therefore, the degeneracies of the peaks in the valence band and at the Γ, N, and P points and along the ΓH and NH lines are 1, 6, 2, 6, and 12, respectively, which add up to 27.[40] The curvatures of effective mass ellipsoids, as shown in the figure, do not present the real values.

In the clathrate compounds, an alkali intercalated atom supplies an electron to the lattice. On the other hand, aliovalent substitutions accept electrons and can compensate for the donated electron by the guest atom. The discussion is extendible to alkaline-earth metal intercalated clathrate compounds as well. An alkaline-earth metal supplies two electrons when it is encapsulated in the Si framework. However, two group III atoms substituted

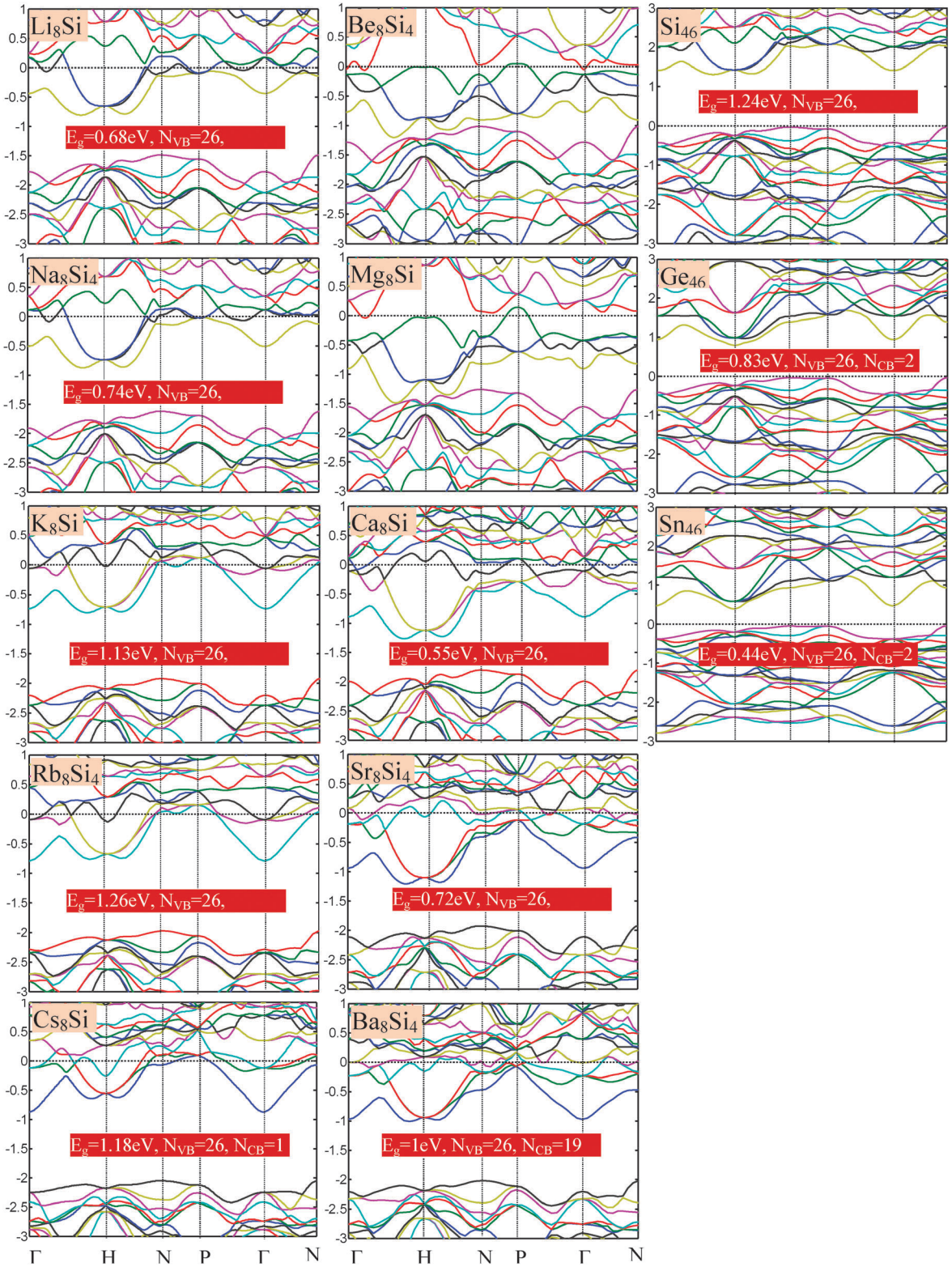

Fig. 2 Electronic band structures for intercalated Si_{46}-VIII with alkali and alkaline-earth metals and pristine type-VIII clathrates Si_{46}, Ge_{46}, and Sn_{46}. The first and second columns represent alkali and alkaline–earth intercalated systems, respectively. The third column of Figures shows the pristine type-VIII clathrates. Each figure displays the energy bands along several symmetry directions of the first Brillouin zone. In the units of $2\pi/a$, the labeled k points correspond to Γ = (0,0,0), H = (1/2,1/2,−1/2), N = (1/2,0,0) and P = (1/4,1/4,1/4). The Fermi level is set to 0 eV and is shown by horizontal dotted line. For all the figures, the Y axis presents energy in eV and the X axis indicates the selected high symmetry path in the Brillouin zone, which is Γ–H–N–P–Γ–N. For all intercalated systems the Fermi level is inside the bands.

in the Si framework can compensate for those two electrons. In order to obtain a desired carrier concentration, the number of supplied and compensated electrons determined by the guest and the substitutional atoms, respectively, should be adjusted appropriately. Therefore, one can reach the optimum carrier concentration in clathrates through both the mechanisms of intercalation and substitution. Both intercalation and substitution result in shifting the position of the Fermi level. As long as the Fermi level is not located more than 0.1 eV into the band edge, the shift can be explained by the rigid band approximation.[41] According to the rigid band approximation, as the guest atom is intercalated in the Si framework, the Fermi level is shifted upward near the conduction band edge. Moreover, if some Si sites in this intercalated Si framework are substituted by group III atoms, a downward shift of the Fermi level is expected. Such a Fermi level shift has been observed in some theoretical studies of type-VIII and type-I Si clathrates.[42,43]

It is interesting to know that in the theoretically investigated Si clathrates, the formation energy of the ones those are simultaneously intercalated and substitutionally co-doped is lower than that of each individually doped clathrate.[42] This property can be attributed to the strong bonding between donors and acceptors. The calculated electronic band structures of alkali (Li, Na, K, Rb, Cs) and alkaline-earth (Be, Mg, Ca, Sr, Ba) intercalated structures along with that of elemental type-VIII clathrates, such as Si_{46}, Ge_{46}, and Sn_{46}, have been presented in Fig. 2. The horizontal dotted lines show the Fermi energy and vertical dashed lines correspond to Γ, H, N, P, and Γ points in k-space. As it is evident from Fig. 2, all the calculated band structures, except Be_8Si_{46} and Mg_8Si_{46} compounds, are qualitatively similar.

The indirect band gaps of Ge_{46} and Sn_{46} are smaller than that of Si_{46} and are equal to 0.83 and 0.44 eV, respectively. The guest atoms shift the Fermi energy into the conduction band and, except for the two cases of Be_8Si_{46} and Mg_8Si_{46}, weakly influence the band structure. It is interesting to know that Be and Mg are the only two materials in group II that have different crystal structures than the other alkali and alkaline-earth metals. While all the metals in group I and II have cubic structures, Be and Mg have hexagonal structures. Our calculations show that among the selected Si_{46}-VIII clathrates, the Fermi energy of only the pristine Si_{46}-VIII is a highly degenerate p type material. Interestingly, the Fermi energy of all the intercalated Si_{46}-VIII clathrates is deep inside the conduction band. Therefore, it is possible to adjust the Fermi energy anywhere in the gap by adjusting the number of the guest atoms in a partially filled clathrate structure. Moreover, the intercalated Si_{46}-VIII clathrates are expected to have smaller thermal conductivity due to the guest rattling, and should result in a higher figure-of-merit than the pristine Si_{46}-VIII. We calculated the electronic formation energies for the Si based type-VIII clathrates of interest from the following equations:

$$\Delta H_{el}(\mathrm{Si, Ge, Sn}_{46}) = E_{\mathrm{Si,Ge,Sn}_{46}} - 46E_{\mathrm{Si,Ge,Sn}}$$

$$\Delta H_{el}(\mathrm{A_8Si_{46}}) = E_{\mathrm{A_8Si_{46}}} - 8E_{\mathrm{A}} - 46E_{\mathrm{Si}}.$$

The first equation is for the pristine clathrate and the second equation is for the binary one, in which A refers to the selected alkali and alkaline-earth elements. The reported values are the electronic energies of formation calculated with respect to the standard states of the elements. A negative value indicates that the material formation is energetically favorable compared with the standard state of its components. Therefore, negative energies indicate the ease of material synthesis although materials with positive formation energies may also be synthesized by supplying extra energy to the system to initiate the reaction. A positive value indicates an endothermic reaction in which the compound material is not more stable than the standard state of its components.

Fig. 2 shows the existence of a large number of valence band (VB) peaks and conduction band (CB) valleys near the band edges of Si_{46}-VIII. The number of carrier pockets near the VB edge is especially very large. This number for Si_{46}-VIII is 26, which is much higher than the best known thermoelectric materials such as $(Bi,Sb)_2T_3$ based alloys, *i.e.* equal to 18, or p-type $Si_{0.8}Ge_{0.2}$ alloys, *i.e.* equal to 6. Herein, we assume that the valleys (or peaks) with $k_BT < 100$ meV away from the band edge can contribute in transport. This number for the CB of Si_{46}-VIII is 19, which is again the largest value among all the known good thermoelectric materials.

According to the results shown in Fig. 2, the intercalation affects the conduction band of Si_{46}-VIII more than its valence band. The intercalation with Li and Na shifts the Γ point in the conduction band (CB) upwards. This reduces the electron pockets from 19 to 18 in these materials. However, the intercalation with K, Rb, and Cs moves the Γ point in the CB down towards the mid gap. For these three alkali atoms, the higher the atomic number, the higher the shift of the Γ point. For the case of intercalation with K and Cs, the Γ point approaches the minimum of the CB and the number of carrier pockets increases to 19. However, in Cs_8Si_{46}-VIII, the downward shift is so significant that the Γ point becomes the CB minimum and the number of carrier pockets reduces to 1. Therefore, Cs_8Si_{46}-VIII is not expected to have a high n-type power factor.

Among all the alkali and alkali earth atoms, intercalations with Be and Mg are exceptions as they result in totally different band structures than that of Si_{46}-VIII. It is also interesting to note that Be and Mg have hexagonal crystal structures, which is different from all the other alkali and alkali earth materials which have cubic structures. The intercalation with the other alkali earth atoms (Ca, Sr, Ba) will not affect the band structure noticeably although similar shift in Γ point is observed. Similar to the case of alkali intercalation, as the atomic mass of the intercalated atom increases, the shift of the Γ point towards the mid gap increases. Among these compounds, Ba_8Si_{46}-VIII shows a higher alignment of the Γ point with other valleys at the CB edge. It should be noted that even though the degeneracy of Γ point is 1, it has a smaller effective mass that can enhance the electron mobility.

Comparing the band structure of Sn_{46}-VIII and Ge_{46}-VIII with that of Si_{46}-VIII, we note that they both have smaller band-gaps and largely reduced number of carrier pockets in the CB,

i.e. 2. The main reason for such a large reduction in the number of electron carrier pockets seems to be due to the convergence of the two valleys at the *ΓH* and *NH* lines in Si_{46}-VIII forming a single valley at the *H* point. The two valleys in the *ΓH* and *NH* lines have large degeneracies of 6 and 12, respectively. They are seen in all the Si_{46}-VIII based clathrates, indicating that they originate from the atomic structure of Si.

Comparing the valence bands of Sn_{46}-VIII, Ge_{46}-VIII, and Si_{46}-VIII (and its derivatives), we note that they all have a similar structure. They all have indirect band gaps and have 26 hole pockets near their VB edges.

The main structural and band structure parameters calculated for the studied clathrate materials are presented in Table 2.

It can be seen that all the intercalated compounds are heavily metallic. However, for thermoelectric applications, a carrier concentration reduction is necessary. To address this issue, we studied the partial intercalation of Na_xSi_{46}, as an example. The calculations showed negligible change in band structure; however, the Fermi energy changed substantially. Fig. 3 shows the calculation of the Fermi energy in Na_xSi_{46} *versus* the Na fraction. It can be seen that the Fermi energy can shift up to 1.54 eV at $x = 0.5$ compared to pure Si_{46}, which is a p-type material. In practice, it is expected that a Na amount of less than 1% will result in an optimum Fermi energy for an n-type material, which will be discussed in Fig. 4. Since DFT is a zero temperature calculation, the Fermi energy at room temperature or higher, which is of interest for TE applications, will be different than that of the zero temperature. However, the plot shows the trend of the reduction of the Fermi energy as the number of Na atoms reduces.

It is also notable that by increasing the temperature, the Fermi function is broadened; hence, the probability of occupying higher energy states is increased, which leads to a shift in the optimum Fermi energy. Fig. 4 represents the thermal

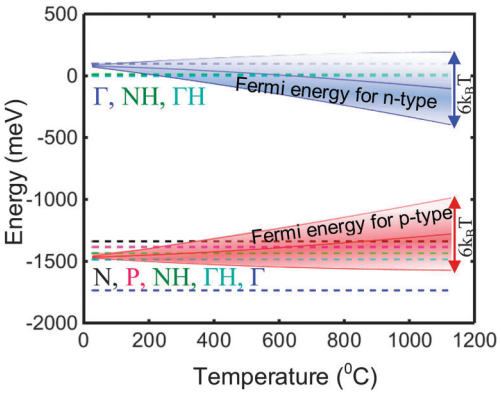

Fig. 4 Broadening of Fermi energies in both n-type and p-type Si_{46}-VIII clathrates. The label letters are colored with the same color of each individual band.

Table 2 The predicted values of the lattice constants, formation energies and fundamental band gaps for the Si based type-VIII clathrates

Type-VIII clathrate	Lattice constant (Å)	Formation energy (kJ mol^{-1})	Band gap (eV)	Density (g cm^{-3})	VB degeneracy	CB degeneracy
Si_{46}	10.10	7.9	1.24	2.082	26	19
Ge_{46}	10.674	7.349	0.83	4.561	26	2
Sn_{46}	12.274	5.920	0.44	4.904	26	2
Li_8Si_{46}	10.1	159.80	0.68	2.171	26	18
Na_8Si_{46}	10.17	81.57	0.74	2.329	26	18
K_8Si_{46}	10.29	84.95	1.13	2.444	26	19
Rb_8Si_{46}	10.375	201.358	1.26	2.937	26	19
Cs_8Si_{46}	10.45	286.78	1.18	3.424	26	1
Be_8Si_{46}	10.08	1166.54	—	2.212	—	—
Mg_8Si_{46}	10.12	287.14	—	2.381	—	—
Ca_8Si_{46}	10.177	−73.41	0.55	2.54	26	18
Sr_8Si_{46}	10.276	−112.76	0.72	3.05	26	18
Ba_8Si_{46}	10.385	−97.17	1	3.7	26	19

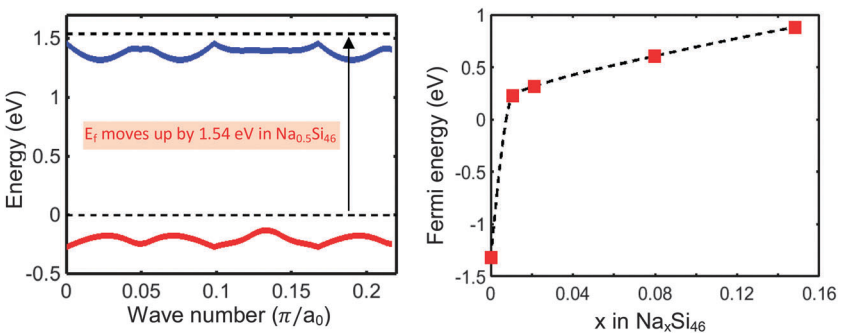

Fig. 3 Intercalation of alkali and alkaline–earth atoms makes a shift in the Fermi energy of clathrate Si_{46}-VIII. The left panel demonstrates the shift in Fermi level due to the intercalation of eight Na atoms. The right panel shows how adding the Na atoms to clathrate Si_{46}-VIII places the Fermi energy deeper into the conduction band. The squares correspond to 0.5, 1, 4, and 8 Na atoms in the unit cell. The zero energy in this plot is the conduction band edge of Si_{46}-VIII.

broadening of the Fermi distribution in both n-type and p-type Si_{46}-VIII clathrates along with the shift of the Fermi energy towards the center of the energy gap. The width of the thermal broadening in the figure is $6k_BT$, which is for demonstration. In the numerical calculations, the energy integrals were calculated up to $20k_BT$ above the Fermi energy for higher accuracy. It is evident from Fig. 4 that three conduction bands and 5 valence bands contribute to the transport.

We will continue to focus on the charge transport properties of Si_{46}-VIII in this study and leave the properties of the other materials for future studies.

Comparison of the major thermoelectric properties of crystalline Si_{46}-VIII

Fig. 5 presents a comparison between the electrical conductivity and the Seebeck coefficient of the Si_{46}-VIII clathrate for both p-type and n-type materials. The primary point is that the electrical conductivity and the Seebeck coefficient have consistent behavior. The Seebeck coefficient of p-type Si_{46}-VIII is higher than that of the n-type due to the presence of more valleys in the valence band close to the Fermi level. Interestingly, the electrical conductivity of p-type Si_{46}-VIII is also higher than that of n-type Si_{46}-VIII, which is due to the smaller effective mass of holes in this material system.

It is observed that as the temperature increases, the discrepancy decreases and diminishes at 1000 °C. With the increase in temperature, the thermal broadening increases and changes the contribution of the valleys in the valence and conduction bands. As it can be seen in Fig. 5(a), the electrical conductivity decreases smoothly with temperature and does not show a bipolar conduction at high temperature, which is due to the large band gap of the material.

The majority carrier concentration has its maximum value at the lower temperature region and does not change clearly with increasing temperature. Fig. 5(b) shows the Seebeck coefficient variation as a function of temperature for crystalline Si_{46}-VIII. Consistent with the behavior of the electrical conductivity, the Seebeck coefficient increases continuously with temperature. The unchanged slope of the Seebeck coefficient curve in higher temperature regions can be attributed to the relatively large band gap of Si_{46}-VIII, which prevents bipolar conduction. The bipolar effect is expected to be more pronounced in Ge_{46}-VIII and Sn_{46}-VIII clathrates due to their smaller band gaps, which would lead to the reduction of high temperature thermoelectric power factors.

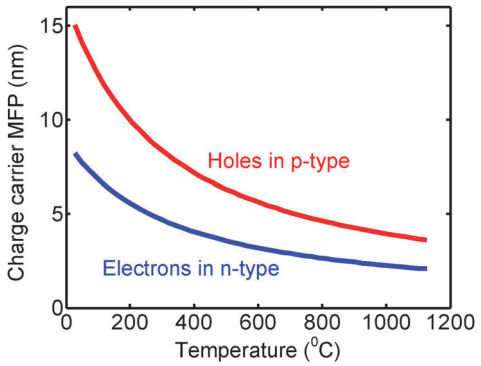

Fig. 6 The mean free path of the majority charge carriers *versus* temperature for Si_{46}-VIII with an optimum doping concentration of 1.1×10^{21} cm^{-3}.

The carrier mean free path (MFP) *versus* temperature has been presented in Fig. 6. Temperature increments from room temperature to 1000 °C lead to a ~65–70% reduction in the MFP of electrons and holes, which can be attributed to the increased scattering of the charge carriers by acoustic phonons.

The predicted accumulated electrical conductivity for p-type Si_{46}-VIII (calculated at T = 1000 °C) has been presented in Fig. 7 as a function of wavelength. It is evident from Fig. 7 that the electrons and holes have a similar range of wavelengths, and that conduction happens dominantly by the ones with a wavelength of 1–3 nm and the smallest wavelength is comparable with the size of the unit cell.

The mobility behavior of Si_{46}-VIII

Both the electron and hole mobilities are mainly affected by ionized impurities and acoustic phonon scatterings. At low temperature, the ionized impurity scattering is dominant. At high temperature, the acoustic phonons become dominant, which explains the mobility reduction with the increase of temperature. The calculated Hall mobility *versus* temperature in Fig. 8 clearly depicts that the amount of Hall mobility is very low for both the types of charge carriers.

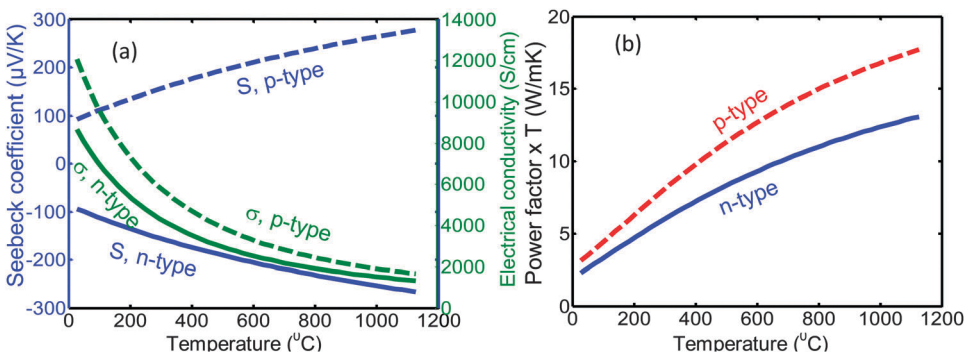

Fig. 5 (a) Electrical conductivity and Seebeck coefficient *versus* temperature and (b) power factor (PFT) for both p-type and n-type Si_{46}-VIII materials at a doping concentration of 1.1×10^{21} cm^{-3}.

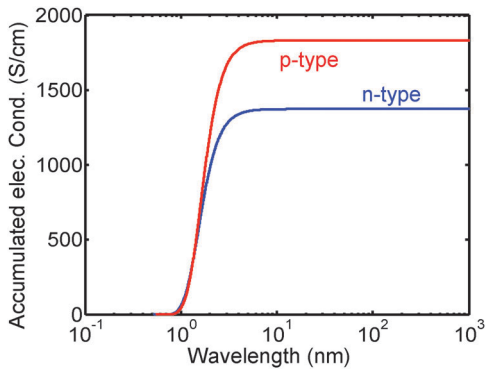

Fig. 7 Accumulated electrical conductivity for p-type (red) and n-type (blue) crystalline Si_{46}-VIIIversus the carrier wavelength at 1000 °C at N_A = 1.1 × 10^{21} cm^{-3}. The charge carriers that contribute dominantly in the conductivity have wavelength smaller than a few nanometers, which is comparable with the size of the unit cell.

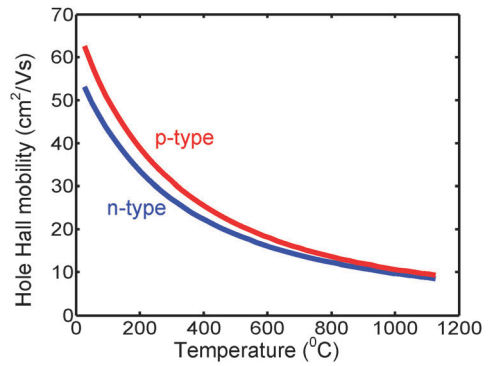

Fig. 8 Hall mobility *versus* temperature for p-type (red) and n-type (blue) Si_{46}-VIII.

Lorentz number

The total thermal conductivity of the material consists of lattice and electronic parts. In highly doped semiconductors, the contribution of charge carriers can be significant and increase the thermal conductivity. The electronic thermal conductivity can be calculated from the Lorentz number. The Lorentz number can be approximated using the Wiedemann–Franz law by L = 2.44 × 10^{-8} WΩ K^{-2}. However, the approximation error can be large and quite often cannot explain the experimental data.[44] It has been discussed that if a material has a very sharp electronic density of states near the Fermi level, the Wiedemann–Franz law is violated and the Lorentz number becomes smaller than its theoretical value.[43] This can occur in strongly correlated materials in which the Wiedemann–Franz law is no longer valid or materials with tightly bound electronic f orbitals such as $YbAl_3$.[45] Moreover, the concept of resonant levels[46] or tuning the doping concentration and layer thickness in superlattices can be also exploited to implement this method for reducing the Lorentz number.[47] Our calculation of the Lorentz number of Si_{46}-VIII also revealed a reduced Lorentz number for this material, which decreases with temperature.

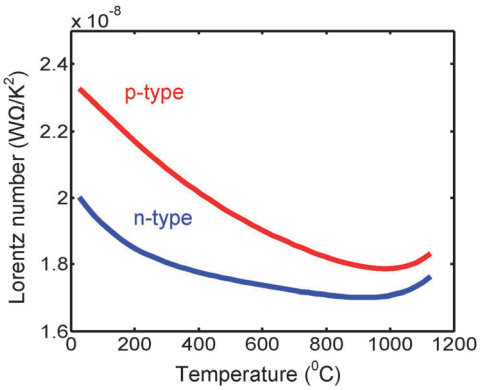

Fig. 9 Lorentz number *versus* temperature for p-type (red) and n-type (blue) Si_{46}-VIII.

Fig. 9 exhibits the Lorentz number *versus* temperature for both p-type and n-type Si_{46}-VIII. For temperatures above 800 °C, the Lorentz number increases and the calculated value at 1000 °C amounts to ~1.82 × 10^{-8} WΩ K^{-2}, which is nearly 30% smaller than the theoretical value for the parabolic energy band of free electrons, *i.e.* 2.44 × 10^{-8} WΩ K^{-2}.

V. Conclusion

The electronic band structure of alkali and alkaline-earth intercalated type-VIII Si clathrates as well as pristine type-VIII Si_{46}, Ge_{46}, and Sn_{46} clathrates were investigated by DFT-GGA. The band structure considerations indicated that all these materials, except $BeSi_{46}$-VIII and $MgSi_{46}$-VIII, have favorable band structures for thermoelectric applications. In particular, our calculation of the thermoelectric properties of Si_{46}-VIII predicted a giant thermoelectric power factor. We applied a semi-classical multi-band model that utilized first principal calculated input parameters to derive the thermoelectric transport properties, including the Seebeck coefficient and the electrical conductivity *versus* temperature. The effect of temperature and doping concentration on the thermoelectric properties of Si_{46}-VIII were investigated using a multi-band Boltzmann transport equation within a relaxation time approximation. The effect of temperature variation on some other transport properties, such as the charge carrier MFPs, Hall mobility, and Lorentz number, were studied for p-type and n-type Si_{46}-VIII. Our calculations showed that charge carriers with wavelengths comparable to the size of the unit cell dominantly contribute in electrical conduction. We also predicted the reduction of the Lorentz number in both p-type and n-type Si_{46}-VIII, which would be beneficial for enhancing ZT. Therefore, Si_{46}-VIII is a promising parent material for thermoelectric applications. Among these materials, Ca_8Si_{46}, Sr_8Si_{46}, and Ba_8Si_{46} have negative formation energies, which indicate their ease of synthesis compared to the others. The intercalation with alkali and alkaline-earth atoms, except Mg and Be, weakly affects the band structure; however, it can significantly reduce the thermal conductivity due to the rattling effect. Therefore, the combination of the predicted giant power

factor and the reduction of the thermal conductivity should result in a large thermoelectric figure-of-merit.

Acknowledgements

This study is partially based upon the work supported by Army Research Office under grant no. W911NF-13-1-0472, and the National Science Foundation (NSF) under grant numbers ECCS-1351533 and CMMI-1363485. The authors would like to thank the Tandy supercomputer center for the many hours of computing time.

References

1 J. L. Cohn, G. S. Nolas, V. Fessatidis, T. H. Metcalf and G. A. Slack, *Phys. Rev. Lett.*, 1999, **82**, 779.
2 G. S. Nolas, J. L. Cohn, G. A. Slack and S. B. Schujman, *Appl. Phys. Lett.*, 1998, **73**, 178180.
3 G. S. Nolas, M. Beekman, J. Gryco, G. A. Lamberton, Jr., T. M. Tritt and P. F. McMillan, *Appl. Phys. Lett.*, 2003, **82**, 910.
4 H. Fukuoka, J. Kiyoto and S. Yamanaka, *Inorg. Chem.*, 2003, **42**, 2933.
5 M. Imai, K. Nishida, T. Kimura and K. Yamada, *J. Alloys Compd.*, 2002, **335**, 270.
6 J. Dong and O. F. Sankey, *J. Phys.: Condens. Matter*, 1999, **11**, 6129.
7 G. S. Nolas, J. L. Cohn, J. S. Dyck, C. Uher and J. Yang, *Phys. Rev. B: Condens. Matter Mater. Phys.*, 2002, **65**, 165201.
8 G. S. Nolas, D. G. Vanderveer, A. P. Wilkinson and J. L. Cohn, *J. Appl. Phys.*, 2002, **91**, 8970.
9 K. Biswas and C. W. Myles, *Phys. Rev. B: Condens. Matter Mater. Phys.*, 2007, **75**, 245205.
10 K. Biswas and C. W. Myles, *Phys. Rev. B: Condens. Matter Mater. Phys.*, 2006, **74**, 115113.
11 J. S. Kasper, P. Hagenmuller, M. Pouchard and C. Cros, *Science*, 1965, **150**, 1713.
12 B. C. Sales, B. C. Chakoumakos, R. Jin, J. R. Thompson and D. Mandrus, *Phys. Rev. B: Condens. Matter Mater. Phys.*, 2001, **63**, 245113.
13 Y. Sasaki, K. Kishimoto, T. Koyanagi, H. Asada and K. Akai, *J. Appl. Phys.*, 2009, **105**, 073702.
14 S. Deng, Y. Saiga, K. Kajisa and T. Takabatake, *J. Appl. Phys.*, 2011, **109**, 103704.
15 K. Kishimoto, N. Ikeda, K. Akai and T. Koyanagi, *Appl. Phys. Express*, 2008, **1**, 031201.
16 W. Carrllo-Cabrera, R. Cardoso Gil and Y. Grin, *Z. Kristallogr. – New Cryst. Struct.*, 2002, **217**, 179.
17 M. Imai, K. Nishida, T. Kmura and K. Yamada, *J. Alloys Compd.*, 2002, **335**, 270.
18 K. Suekuni, M. A. Avila, K. Umeo and T. Takabatake, *Phys. Rev. B: Condens. Matter Mater. Phys.*, 2007, **75**, 195210.
19 P. Norouzzadeh, C. W. Myles and D. Vashaee, *J. Phys.: Condens. Matter*, 2013, **25**(47), 475502.
20 G. S. Nolas, J. M. Ward, J. Gryko, L. Qiu and M. A. White, *Phys. Rev. B: Condens. Matter Mater. Phys.*, 2001, **64**, 153201.
21 J. L. Cohn, G. S. Nolas, V. Fessatidis, T. H. Metcalf and G. A. Slack, *Phys. Rev. Lett.*, 1999, **82**, 779.
22 K. Biswas and C. W. Myles, *Phys. Rev. B: Condens. Matter Mater. Phys.*, 2007, **75**, 245205.
23 S. Saito and A. Oshiyama, *Phys. Rev. B: Condens. Matter Mater. Phys.*, 1995, **51**, 2628.
24 V. I. Smelyanski and J. S. Tse, *Chem. Phys. Lett.*, 1997, **264**, 459.
25 P. Mélinon, *et al.*, *Phys. Rev. B: Condens. Matter Mater. Phys.*, 1998, **58**, 12590.
26 K. Moriguchi, S. Munetoh and A. Shintani, *Phys. Rev. B: Condens. Matter Mater. Phys.*, 2000, **62**, 7138; K. Moriguchi, M. Yonemura, A. Shintani and S. Yamanaka, *Phys. Rev. B: Condens. Matter Mater. Phys.*, 2000, **61**, 9859.
27 S. Paschen, W. Carrillo-Cabrera, A. Bentien, V. H. Tran, M. Baenitz, Y. Grin and F. Steglich, *Phys. Rev. B: Condens. Matter Mater. Phys.*, 2001, **64**, 214404.
28 A. Bentin, V. Pacheco, S. Paschen, Y. Grin and F. Steglich, *Phys. Rev. B: Condens. Matter Mater. Phys.*, 2005, **71**, 165206.
29 G. K. H. Madsen, K. Schwarz, P. Blaha and D. J. Singh, *Phys. Rev. B: Condens. Matter Mater. Phys.*, 2003, **68**, 125212.
30 K. Kishimoto, N. Ikeda, K. Akai and T. Koyanagi, *Appl. Phys. Express*, 2008, **1**, 031201.
31 A. Bentien, V. Pacheco, S. Paschen, Y. Grin and F. Steglich, *Phys. Rev. B: Condens. Matter Mater. Phys.*, 2005, **71**, 165206.
32 W. Carrllo-Cabrera, R. Cardoso Gil and Y. Grin, *Z. Kristallogr. – New Cryst. Struct.*, 2002, **217**, 179.
33 G. Kresse and J. Hafner, *Phys. Rev. B: Condens. Matter Mater. Phys.*, 1993, **47**, 558; G. Kresse and J. J. Furthmüller, *Phys. Rev. B: Condens. Matter Mater. Phys.*, 1996, **54**, 11169.
34 J. P. Perdew, K. Burke and M. Ernzerhof, *Phys. Rev. Lett.*, 1996, **77**, 3865.
35 G. Kresse and J. Hafner, *J. Phys.: Condens. Matter*, 1994, **6**, 8245.
36 H. Shi, D. Parker, M.-H. Du and D. J. Singh, *Phys. Rev. Appl.*, 2015, **3**, 014004.
37 We used the Vienna Ab initio Simulation Program (VASP), developed at the Institut für Theoretische Physik of the Technische Universität Wien. G. Kresse and J. Furthmüller, *Comput. Mater. Sci.*, 1996, **6**, 15.
38 G. Kresse and J. Hafner, *Phys. Rev. B: Condens. Matter Mater. Phys.*, 1993, **47**, 558; G. Kresse and J. J. Furthmüller, *Phys. Rev. B: Condens. Matter Mater. Phys.*, 1996, **54**, 11169.
39 MedeA: Materials Exploration and Design Analysis, version 2.14.6; Material Design, Inc.: Angel Fire, NM, 1998–2014; http://www.materialsdesign.com.
40 P. Norouzzadeh, C. W. Myles and D. Vashaee, *Sci. Rep.*, 2014, **4**, 7028.
41 L. Zhang and D. J. Singh, *Phys. Rev. B: Condens. Matter Mater. Phys.*, 2009, **80**, 075117.
42 P. Norouzzadeh, C. W. Myles and D. Vashaee, *J. Alloys Compd.*, 2014, **587**, 474.

43 K. Nakamura, S. Yamada and T. Ohnuma, *Mater. Trans.*, 2013, **54**, 3.
44 G. Chen, *Nanoscale Energy Transport and Conversion*, Oxford University Press, New York, 2005.
45 G. D. Mahan and J. O. Sofo, *Proc. Natl. Acad. Sci. U. S. A.*, 1996, **93**, 7436.
46 J. P. Heremans, V. Jovovic, E. S. Toberer, A. Saramat, K. Kurosaki, A. Charoenphakdee, S. Yamanaka and G. J. Snyder, *Science*, 2008, **321**, 554.
47 Z. Bian, M. Zebarjadi, R. Singh, Y. Ezzahri, A. Shakouri, G. Zeng, J. H. Bahk, J. E. Bowers, J. M. O. Zide and A. C. Gossard, *Phys. Rev. B: Condens. Matter Mater. Phys.*, 2007, **76**, 205311.